Journal of Bone and Mineral Research, 2024, **39**, 1025–1041
https://doi.org/10.1093/jbmr/zjae072
Advance access publication: May 9, 2024
Research Article

Osteomodulin deficiency in mice causes a specific reduction of transversal cortical bone size

Wenbo Zhao[1], Simon von Kroge[1], Jelena Jadzic[2], Petar Milovanovic[2], Praveer Sihota[1], Julia Luther[1], Laura Brylka[1], Felix N. von Brackel[1], Ernesto Bockamp[3], Björn Busse[1], Michael Amling[1], Thorsten Schinke[1,*,†], Timur A. Yorgan[1,*,†]

[1]Department of Osteology and Biomechanics, University Medical Center Hamburg-Eppendorf, D-20246 Hamburg, Germany
[2]Center of Bone Biology, Institute of Anatomy, Faculty of Medicine, University of Belgrade, Belgrade 11000, Serbia
[3]Institute of Translational Immunology (TIM), University Medical Center, Johannes Gutenberg-University Mainz, D-55131 Mainz, Germany
*Corresponding author: Timur A. Yorgan, or Thorsten Schinke, Department of Osteology and Biomechanics, University Medical Center Hamburg Eppendorf, Martinistrasse 52, D-20246 Hamburg, Germany (t.yorgan@uke.de or schinke@uke.de).
[†]Thorsten Schinke and Timur A. Yorga jointly supervised this work.

Abstract

Skeletal growth, modeling, and remodeling are regulated by various molecules, one of them being the recently identified osteoanabolic factor WNT1. We have previously reported that WNT1 transcriptionally activates the expression of *Omd*, encoding Osteomodulin (OMD), in a murine mesenchymal cell line, which potentially explained the skeletal fragility of mice with mutational WNT1 inactivation, since OMD has been shown to regulate type I collagen fibril formation in vitro. In this study we confirmed the strong induction of *Omd* expression in a genome-wide expression analysis of transfected cells, and we obtained further evidence for *Omd* being a direct target gene of WNT1. To assess the in vivo relevance of this regulation, we crossed *Omd*-deficient mice with a mouse line harboring an inducible, osteoblast-specific *Wnt1* transgene. After induction of *Wnt1* expression for 1 or 3 weeks, the osteoanabolic potency of WNT1 was not impaired despite the *Omd* deficiency. Since current knowledge regarding the in vivo physiological function of OMD is limited, we next focused on skeletal phenotyping of wild-type and *Omd*-deficient littermates, in the absence of a *Wnt1* transgene. Here we did not observe an impact of *Omd* deficiency on trabecular bone parameters by histomorphometry and μCT either. Importantly, however, male and female *Omd*-deficient mice at the ages of 12 and 24 weeks displayed a slender bone phenotype with significantly smaller long bones in the transversal dimension, while the longitudinal bone growth remained unaffected. Although mechanical testing revealed no significant changes explained by impaired bone material properties, atomic force microscopy of the femoral bone surface of *Omd*-deficient mice revealed moderate changes at the nanostructural level, indicating altered regulation of collagen fibril formation and aggregation. Taken together, our data demonstrate that, although OMD is dispensable for the osteoanabolic effect of WNT1, its deficiency in mice specifically modulates transversal cortical bone morphology.

Keywords: bone matrix, cortical bone diameter, osteoblast, Osteomodulin, WNT1

Lay Summary

We explored the physiological relevance of the protein Osteomodulin (OMD) that we previously found to be induced by the osteoanabolic molecule WNT1. While other studies have shown that OMD is involved in the regulation of collagen fibril formation *in vitro*, its function *in vivo* has not been investigated. We confirmed that OMD is directly regulated by WNT1 but surprisingly, when we bred mice lacking OMD with mice engineered to highly express WNT1, we found that the osteoanabolic effect of WNT1 was unaffected by the absence of OMD. Interestingly, mice lacking OMD did show differences in the shape of their bones, particularly in their width, despite no significant changes in bone density or length. Investigation of the bone matrix of mice lacking OMD at the nanostructural level indicated moderate differences in the organization of collagen fibrils. This study provided further insights into the effect of WNT1 on bone metabolism and highlighted a specific function of OMD in skeletal morphology.

Introduction

Skeletal growth, modeling, and remodeling are highly complex processes involving different cell types with unique functions. Whereas growth plate chondrocytes are primarily responsible for the elongation of skeletal elements, bone-forming osteoblasts and bone-resorbing osteoclasts are not only essential during skeletal development and growth, but are also continuously active in a life-long process of bone remodeling, which is a prerequisite for long-term skeletal integrity.[1-3] If the delicate balance required for physiological bone remodeling is shifted toward bone resorption, the result is a progressive loss of bone mass. This leads to the subsequent reduction of structural integrity and mechanical strength that manifests itself as osteoporosis, one of the most prevalent and detrimental disorders in the elderly population.[4] While there are several treatment options available, there are important limitations regarding the suitability for each individual patient, and a deeper understanding of the molecular mechanisms controlling bone modeling and remodeling is required to identify and establish new therapeutic approaches.[5]

Received: December 19, 2023. **Revised:** April 26, 2024. **Accepted:** May 8, 2024

WNT1, a member of the WNT family of ligands, has been recently established as a signaling molecule with a high osteoanabolic activity. We have previously shown that the osteoblast-specific transgenic induction of *Wnt1* in mice leads to a rapid and extensive increase in bone mass.[6] On the other hand, it has been shown that monoallelic or biallelic pathogenic variants of *WNT1* can cause early-onset osteoporosis and osteogenesis imperfecta type XV, respectively.[7-10] These findings were further supported by the analysis of mouse models harboring specific *Wnt1* variants observed in affected patients, as well as animals with osteoblast-specific deletion of *Wnt1*.[6,11-14] In both approaches a distinct loss of skeletal integrity was observed. Furthermore, during the skeletal analysis of mice harboring the G177C variant of WNT1, which causes osteogenesis imperfecta type XV, we observed that not only bone mass, but also bone matrix quality was negatively affected.[12] While the exact molecular mechanisms leading to the observed change of bone matrix properties remained to be elucidated, we identified *Omd* as a potential WNT1 target gene. Indeed, treatment of mesenchymal ST2 cells with recombinant WNT1 led to a marked induction of *Omd* transcription, and bone protein extracts from *Wnt1*^{G177C} animals displayed decreased OMD content.[12]

Osteomodulin (OMD, also known as osteoadherin) is a proteoglycan located in the bone matrix where it can bind to the mineral phase of bone, ie, hydroxyapatite.[15] In vitro evidence indicates that OMD interacts with type I collagen and can modulate collagen fibril thickness. More specifically, OMD was described to reduce the diameter and alter the morphology of collagen fibrils.[16] On a molecular level the interaction of OMD with type 1 collagen is presumed to slow the rapid self-assembly of collagen fibers and allow for the formation of more compact and thus more robust and stable structures.[17] Furthermore, data from in vitro studies involving osteoblast cell lines and odontoblasts indicate that OMD has a direct effect on these cell types, promoting viability, differentiation, and suppressing proliferation.[18-21] Additionally, it was recently demonstrated in a bone defect model that OMD interacts with BMP2 to potentiate its osteoanabolic effect.[21] While these results suggest an important function of OMD in bone formation and osteoblast biology, the in vivo relevance has not been fully explored to date. Only recently a first study was published, where it was shown that loss of OMD in mice negatively impacts articular and growth plate cartilage, while only moderate effects on bone microarchitecture were observed.[22] Moreover, *Bglap*-driven overexpression of *Omd* caused accelerated longitudinal bone growth, but negatively influenced trabecular bone mass.[22]

In our study we set out to investigate if OMD is required for the osteoanabolic effect of WNT1 by combining an inducible, osteoblast-specific *Wnt1* transgene with *Omd*-deficient mice. Additionally, we explored the physiological role of OMD in bone formation and remodeling by careful and thorough skeletal phenotyping of an *Omd*-deficient mouse model and compared with wild-type littermates.

Materials and methods

Animal husbandry and experiments

Omd-deficient mice (B6;129S5-*Omd*^{tm1Lex}/Uke) were obtained as frozen sperm from the MMRC repository (011749-UCD) and revitalized in our animal facility according to standard protocols. The mice were bred on a C67Bl6/J background. In this mouse line *Omd* was inactivated via gene trap technique in embryonic stem cells by the MMRC-contributor Lexicon Pharmaceuticals, Inc. Genotyping was performed using primer pairs for the wild-type (WT) (5'-GAT GCC CTG GAA CTT ACT ATG C-3'; 5'-GTA CTC CCT CGG CCA CTA TCT GC-3') and knockout (KO) allele (5'-TCC CCC ATT GTC TCA TGT CC-3'; 5'-GCA GCG CAT CGC CTT CTA TC-3') resulting in a 218 bp WT and 286 bp KO PCR product.

Wnt1-transgenic/*Omd*-deficient mice (STOCK-Tg(tetO-*Wnt1*,-luc)TWNTLach-Tg(Col1a1-tTa)139Niss-*Omd*^{tm1Lex}/Uke) were generated by crossing osteoblast-specific inducible *Wnt1*-transgenic mice with Omd-deficient mice.[6,23,24] Genotyping of the *Wnt1*-transgenic mice was performed as previously described.[6] Unless indicated otherwise, mice from the *Wnt1*-transgenic and *Wnt1*-transgenic/*Omd*-deficient line were kept under a doxycycline-containing diet (ssniff-Spezialdiäten GmbH, DE). All mice were kept in a specific pathogen-free environment with a 12-h light/dark cycle, 45%–65% relative humidity, and 20–24 °C ambient temperature in open or individually ventilated cages with wood shavings bedding and nesting material in groups not surpassing 6 animals/cage. The mice had access to tap water and standard rodent chow (1328P, Altromin Spezialfutter GmbH & Co. KG, DE) *ad libitum* unless specified otherwise. The animals were sacrificed via CO_2 intoxication and body mass and length (base of the skull to root of the tail) were recorded. The skeletons were fixed in 3.7% PBS-buffered formaldehyde for 48 hr prior to storage in 80% ethanol. The number of animals per group was 3 to 7, with the exact number represented by the individual data points in the corresponding figures. All animal experiments were approved by the animal facility of the University Medical Center Hamburg-Eppendorf and by the "Behörde für Soziales, Familie, Gesundheit und Verbraucherschutz" (Org869, Org1091, N022/2022) in accordance with the local implementation of EU Directive 2010/63/EU for animal experiments. No adverse events were observed. A detailed description of the groups of mice used in this study is provided in Table S1.

Cell culture

Primary calvarial osteoblasts were isolated by sequential collagenase-dispase II digestion from the calvariae of 5 days old mice, while bone marrow-derived osteoblasts were obtained from femora, tibiae, and pelves of 10- to 12-week-old mice. Primary osteoblasts were differentiated in the presence of α-Minimum Essential Medium Eagle (α-MEM, Sigma-Aldrich, United States) supplemented with 10% FCS (Thermo Fisher Scientific, United States), 1% penicillin/streptomycin (Thermo Fisher Scientific, United States), 50 μg/ml ascorbic acid, and 10 mM ß-glycerophosphate as previously described.[25] The mesenchymal cell line ST2 (obtained from DSMZ, DE) was cultured in α-MEM (Sigma-Aldrich, United States) supplemented with 10% fetal calf serum (Thermo Fisher Scientific, United States) and 100 U/ml penicillin/streptomycin (Thermo Fisher Scientific, United States). Alizarin red staining was performed and quantified as previously described.[26]

Transfection

ST2 cells were transfected with the previously described pLNCX-based expression plasmids containing either the wild-type *Wnt1* open reading frame or a variant encoding the G177C mutation that has been shown to cause osteogenesis

imperfecta type XV.[12] For transfection the Lipofectamine 2000 system (Thermo Fisher Scientific, United States) was used with 1 μg of plasmid DNA per well (12 well-format) at 80%–90% confluency. RNA was isolated as described below 5 days after transfection.

WNT stimulation of ST2 cells

ST2 cells were cultured to 80%–90% confluency and stimulated with the following recombinant murine WNT ligands administered in FCS- and antibiotic-free α-MEM for 0.5, 2, or 6 hr as indicated prior to RNA isolation: 100 ng/ml recombinant murine WNT1/SFRP1 complex (reWNT1/SFRP1, Bio-Techne, United States), 50 ng/ml recombinant murine SFRP1 (reSFRP1, Bio-Techne, United States) as an equimolar control, 100 ng/ml recombinant murine WNT3a (reWNT3a, Pepro-Tech, United States), and 100 ng/ml recombinant murine WNT5a (reWNT5a, R&D Systems, United States).

Expression analysis

RNA was isolated from cell cultures and tissue using the Nucleospin Kit (Macherey-Nagel, DE) according to manufacturer's instructions. Concentration and quality of RNA were measured using a NanoDrop ND-1000 system (Thermo Fisher Scientific, United States) and the TapeStation 2200 system (Agilent Technologies, United States). For qRT-PCR expression analysis, 500 ng of RNA was reversed transcribed using Verso cDNA Synthesis Kit (Thermo Fisher Scientific, United States) according to manufacturer's instructions. Quantitative expression analysis was performed using a StepOnePlus system and predesigned TaqMan gene expression assays (Applied Biosystems, United States): *Alpl* (Mm00475834_m1), *Apcdd1* (Mm01257559_m1), *Aspn* (Mm00445945_m1), *Bglap1* (Mm03413826_mH), *Col1a1* (Mm00801666_g1), *Omd* (Mm00449589_m1), *Postn* (Mm00450111_m1), *Runx2* (Mm00501580_m1), *Sp7* (Mm00504574_m1), *Tnfrsf11b* (Mm00435454_m1), *Tnfsf11* (Mm00441906_m1), *Wnt16* (Mm00446420_m1). *Gapdh* (4352661) expression was used as an internal control. Expression was reported relative to the internal control or as fold change values according to the $\Delta\Delta C_T$ method as indicated in the figures.

Microarray-based whole transcriptome analysis was performed utilizing the Clariom D mouse assay (Thermo Fisher Scientific, United States) according to the manufacturer's GeneChip™ WT PLUS reagent kit manual (document 703 174, revision A.0). In brief, 100 ng of total RNA per sample pooled from 3 independent experiments per condition was used for the synthesis of second-cycle ss-cDNA. 5 μg per sample of fragmented and labeled cDNA was subsequently used for gene chip hybridization. After washing and staining with Affymetrix Fluidics Station 450, microarrays were scanned with the Affymetrix Gene Chip Scanner 7G. Data were analyzed with Transcriptome Analysis Console software (TAC 4.0, Thermo Fisher Scientific, United States) using default analysis settings (version 2) and Gene + Exon - SST-RMA as summarization. Full datasets have been uploaded to the GEO repository (GSE249300).[27]

Western blot

Proteins were isolated from bone marrow-derived osteoblasts after osteogenic differentiation of 15 days using RIPA buffer or from frozen bones by homogenization in liquid nitrogen and subsequent incubation for 96 hrs in 4 M guanidine buffer followed by centrifugation and concentration of the supernatant that was finally dialyzed against dH_2O. The protein concentration was determined by a commercially available protein assay (Bio-Rad Laboratories, United States). 20 μg of protein per sample were separated in Bolt Mini Gels (12% Bis-Tris, 1.0 mm x 10 well, Life Technologies, United States) with The Bolt MES SDS Running Buffer (Life Technologies, United States) in a Mini Gel Tank system (90 V, 75 min, Life Technologies, United States). The same system was used with Bolt Transfer Buffer (Life Technologies, United States) to transfer the gel onto a Nitrocellulose membrane (0.45 μm pore size, Schleicher & Schuell, United States). 5% BSA in TBST was used for blocking the membrane and diluting the antibodies: Anti-Omd: #AF3308 1:1666 dilution (R&D Systems, United States); Anti β-actin #4967 1:1000 dilution (Cell Signaling Technology, United States); Secondary Rabbit Anti-Goat Immunoglobulins/HRP: #P0449, 1:1000 dilution (Dako GmbH, DK). Pierce ECL Plus Western blotting substrate (1:40 ratio, Thermo Fisher Scientific, United States) was used to detect signals in a Molecular Imager ChemiDoc XRS System (Bio-Rad Laboratories, United States).

Skeletal histology

Lumbar vertebral bodies L1 to L4 and one tibia were extracted from formalin-fixed skeletons and dehydrated in ascending alcohol concentrations. Embedding in methylmetacrylate for undecalcified histology was performed as described previously.[12] Sections of 4 or 12 μm thickness were cut in the sagittal plane on a Microtec rotation microtome (Techno-Med GmbH, DE). These were stained by the von Kossa/van Gieson or Toluidine blue by established procedures described elsewhere.[28] Histomorphometry was performed in a blinded fashion according to the ASBMR guidelines using the Bioquant Osteo histomorphometry system (BIOQUANT Image Analysis, United States) for structural bone microarchitecture analysis or the Osteomeasure system (OsteoMetrics, United States) for cellular and dynamic histomorphometry.[29]

Polarized light microscopy

Circular polarized light imaging was performed on 4 μm undecalcified tibia sections with an Olympus BX53 microscope with polarization filters (Olympus, JP). Using Olympus cellSense Dimension software (v4.1, Olympus, JP), 2 adjacent regions of interest for each medial and lateral cortical bone were imaged beginning 0.7 mm distal of the proximal growth plate. Images were analyzed by ImageJ (v1.54f, National Institutes of Health, United States) by first reducing the images to gray scale and then using the plugin "OrientationJ" (v2.0.5) to measure the coherency of collagen fibers.[30,31]

Quantitative backscattered electron imaging

The bone mineral density distribution of cortical bone in *Omd*-deficient and control mice was determined by quantitative backscattered electron imaging as described previously.[32] Embedded tibiae of 12-week-old female mice were imaged using a backscattered electron detector (Type 202, K.E. Developments Ltd., United Kingdom) attached to a scanning electron microscope (LEO 435, LEO Microscopy Ltd., United Kingdom). A region of interest situated 1-2 mm distal of the proximal growth plate was analyzed at medial and lateral sites. The acquired gray-value based images reflecting the local calcium content were evaluated using a custom-made MATLAB (TheMathWorks, United States) script to derive characteristic determinants of the bone mineral density distribution and osteocyte lacunae.

Radiological assessment

μCT scanning and microarchitectural analysis were performed on extracted femora, skulls, tibiae, and humeri with a voxel resolution of 10 μm at 55 kVp, 145 μA using a μCT 40 desktop conebeam microCT system (Scanco Medical AG, CH) as previously described according to standard guidelines.[33,34] The Scanco MicroCT software suite (v6.5-2, Scanco Medical AG, CH) was used for evaluation. Trabecular bone was analyzed in the distal metaphysis of the femur in a volume situated 2500 to 500 μm proximal of the distal growth plate. Cortical bone was analyzed in a volume with a length of 1000 μm situated in the middle of the femoral diaphysis. Calvarial thickness was determined on segmented 3D models of the skulls in the frontal plane at the second turn of the cochleae. Calvarial porosity was determined in a volume with a length of 3000 μm on the right parietal bone, excluding any sutures at the medial and lateral edges of the parietal bone. Cortical parameters of tibiae were determined in a 1000 μm long section located centrally between the distal end of proximal growth plate and the proximal start of distal tibiofibular connection. For humeri, cortical parameters were determined in a 1000 μm long section beginning 500 μm distal of the diaphyseal midpoint. The inner and outer diameters of cortical bone were calculated from total tissue area and cortical thickness based on a circular shape as the modeling basis.

Biomechanical testing

For biomechanical testing, a 3-point-bending test was performed on the same explanted femora as used for μCT analysis. Testing was performed with a universal testing machine Z2.5/TN1S (Zwick Roell, DE). Femora were horizontally mounted and centrally positioned with the posterior surface facing downward at a support distance of 7 mm. A constant displacement rate of 0.05 mm/s was applied. Load–displacement data were recorded until failure. Results were calculated in the testXpert software (Zwick Roell, DE). To determine the flexural strength and flexural stiffness, structural data, ie, the second moment of area and the section modulus both calculated by the outer and inner diameter, obtained via μCT analysis of the cortical compartment were utilized.

Nanoscale material properties of the bone matrix were analyzed by nanoindentation using an iMicro nanoindenter (KLA instruments, United States) equipped with a Berkovich diamond tip. Prior to testing all embedded specimens were ground to a co-planar finish and surface-polished. The cortical bone of each sample was tested with at 10-20 indentations at a distance of at least 20 μm between each indent. For validation of the indents, ie, correct position and appearance, the integrated microscope was used. Indentations were performed in depth-sensing continuous stiffness mode with a target depth of 3000 nm and a target indentation strain rate of 0.05 s^{-1}. Calibration was carried out on fused silica before and after each measurement. The hardness and elastic modulus were obtained applying a Poisson's ratio of 0.3 based on a previously described method and using the software provided by the manufacturer.[35]

Atomic force microscopy

Samples of the mid-diaphysis cortex of undecalcified mouse femora were fixed onto a sample disk and imaged by Level atomic force microscopy system (Anfatec Instruments AG, DE) under ambient conditions. The images were obtained in high-resolution dynamic (non-contact) scanning mode using a commercial atomic force microscopy cantilever (HQ: NSC15/AlBS, MikroMasch, BG) with a cantilever length of 125 μm, force constant of 40 N/m, resonant frequency around 275 kHz, and tip radius less than 10 nm. The scanning parameters included the field of view of 2x2 μm, image resolution of 256x256 pixels, and a scanning speed of 2 lines/second. To account for heterogeneity of bone nanostructure, at least 10 different imaging sites were analyzed in each mouse. Topography, amplitude, and phase images were obtained simultaneously, which allowed more comprehensive evaluation of the observed nanostructural features. Semiquantitative analysis of various observed nanostructural features/patterns was performed in a blinded fashion by 2 investigators to determine the relative frequency of images containing a particular feature/pattern per mouse. Each image was classified into one of the available categories (eg, heterogenous, intermediate, and homogenous) per parameter (surface homogeneity, density of packing, and parallelism). The percentage of images assigned to each category was calculated per animal and used for further comparisons.

Statistical analysis

All data in the manuscript are presented as individual values as well as means ± standard deviations. Statistical analysis for the comparison of 2 groups was performed by initial testing for equal variance by F-test and subsequent unpaired, 2-tailed Student t-test if there was no difference in variance or Welch t-test if the variance was significantly different. For the comparison of multiple groups ANOVA with Tukey's post-hoc test was used. Chi-squared test was utilized to compare observed vs. expected results. All statistical analysis was performed using Prism software (Graph-Pad Software, United States). *P*-values below 0.05 were considered statistically significant. Sample size and power of analysis for animal experiments was determined by an a priori t-test with G*Power for a significance level α of 0.05 and power of 0.8 based on an estimated effect size.[36]

Results

Although the osteoanabolic function of WNT1 is now well established, the underlying molecular mechanisms have not been fully elucidated. Therefore, we transfected mesenchymal ST2 cells with plasmids containing either the open reading frame of *Wnt1* or the empty pLNCX vector. Whole transcriptome analysis by microarray revealed that *Aspn*, *Postn*, and *Omd* were the most induced genes in *Wnt1*-transfected cells compared with cells transfected with the control plasmid (Figure 1A). We confirmed the induced expression of these 3 genes by qRT-PCR, where we additionally observed an abrogation of this induction when a plasmid containing a hypomorphic variant of *Wnt1* (G177C) was used that has been shown to cause osteogenesis imperfecta type XV (Figure 1B). Since our previously performed genome-wide expression analysis, ie, ST2 cells exposed to a recombinant reWNT1/SFRP1 complex or reSFRP1 alone, also identified *Postn* and *Omd* as WNT1-induced genes, we performed additional experiments to analyze if these genes are direct targets of WNT1.

More specifically, we stimulated ST2 cells with the previously used recombinant reWNT1/SFRP1 complex (or with reSFRP1 alone) for 30 min, 2 hr, and 6 hr and subsequently

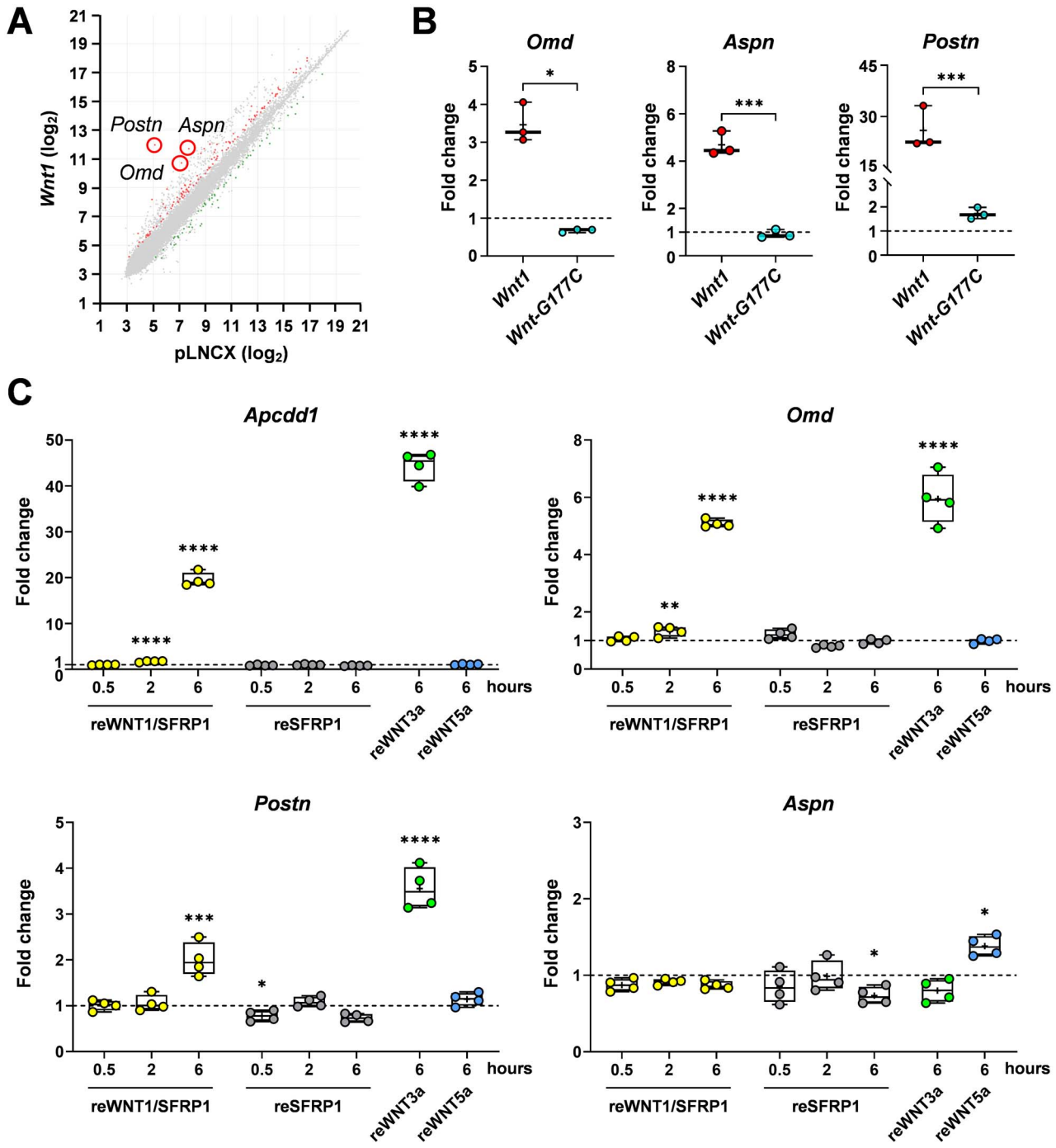

Figure 1. *Omd* is a WNT1-induced gene. A) Scatter plot of microarray expression values. Average signal intensities of transcripts in ST2 cells 5 days after transfection with a *Wnt1* expression plasmid or an empty pLNCX vector are shown with the 3 most differentially expressed genes labeled and marked by circles. B) Confirmation of microarray results by qRT-PCR. Expression of *Omd*, *Aspn*, and *Postn* in ST2 cells 5 days after transfection with a wild-type *Wnt1* expression plasmid or a plasmid encoding the osteogenesis imperfecta-causing G177C variant of *Wnt1* relative to the expression in ST2 cells transfected with the empty pLNCX vector (dashed line). C) Expression of *Apcdd1, Omd*, *Aspn*, and *Postn* in ST2 cells stimulated for the indicated duration with either recombinant WNT1/SFRP1, SFRP1, WNT3a, or WNT5a compared with PBS treated controls (indicated by dashed lines). Data are presented as box plots with dots for individual datapoints. Data were analyzed by Student t-test (B) or one-way ANOVA with Tukey's post-hoc test (C). * $P < .05$, ** $P < .01$, *** $P < .001$, **** $P < .0001$.

monitored gene expression by qRT-PCR. Here we observed that *Omd* was significantly induced after 2 hr of treatment, similar to the established canonical WNT signaling target gene *Apcdd1* (Figure 1C). A stronger induction was observed after 6 hr of reWNT1/SFRP1 administration, also for *Postn*, but not for *Aspn*. To address the question, if this regulation is explained by activated canonical WNT signaling, we additionally administered an established canonical (reWNT3a) and non-canonical (reWNT5a) WNT ligand.[26] Whereas *Apcdd1*, *Omd, and Postn* were induced by reWNT3a, *Aspn* expression was only increased after reWNT5a administration. Taken together, these data confirmed that *Omd* (similar to *Apcdd1*

and *Postn*) is a direct WNT1 target in ST2 cells, whereas the increased expression of *Aspn* in transfected cells is rather a secondary event. In this regard it is also noteworthy that an in silico analysis via ConTra v3[37] of the 1 kb region upstream of the Omd transcription start site indicated the presence of 5 potential binding sites for the canonical Wnt-transcription factors TCF/LEF (Figure S1).

Based on the relatively specific expression of *Omd* in bone tissue (Figure 2A), compared with the expression pattern of *Aspn* and *Postn* (Figure S2), a clear induction of *Omd* throughout osteoblast differentiation (Figure 2B), but also the limited yet intriguing current knowledge regarding the function of OMD in collagen fibril formation, we focused our further research efforts on the role of OMD as a potential downstream target of WNT1. Therefore, we obtained an *Omd*-deficient mouse line and established a colony of these animals. Genotyping by PCR provided unambiguous results (Figure 2C), and the expression of *Omd* in bones isolated from homozygous mice was fully absent (Figure 2D). The allele frequency of mice born from heterozygous matings did not differ significantly from the expected Mendelian ratio (Figure 2E) and we did not observe gross morphological differences as determined by body mass and body length measurements in female $Omd^{-/-}$ mice at the age of 12 and 24 weeks or male $Omd^{-/-}$ mice at the age of 12 weeks, when compared with the respective $Omd^{+/+}$ littermates (Figure 2F).

In order to address the main research question of our study, ie, if the lack of OMD modulates the osteoanabolic effect of WNT1, we crossed the *Omd*-deficient mouse line with a mouse line harboring an inducible (dox-off) osteoblast-specific *Wnt1* transgene. Due to the origin of the investigated animals from different colonies, a direct comparison between littermate mice of all 4 groups was not feasible in this dataset. However, the relative effect of *Wnt1* induction within either the *Omd* wild-type or *Omd*-deficient group resulted in sufficiently reliable evidence. Induction of the *Wnt1* transgene for 1 or 3 weeks until the age of 12 weeks led to the expected progressive increase in trabecular bone mass as determined by histomorphometry of vertebral bodies from female mice. The absence of OMD had no marked influence on this osteoanabolic effect (Figure 3A and B). This finding was additionally confirmed in the tibiae from the same mice, where the accrual of trabecular bone mass in response to *Wnt1* induction was not negatively affected by the lack of OMD (Figure 3C and D). Analysis of the femoral cortical bone showed a significant increase of cortical thickness after 3 weeks of *Wnt1* induction independent of the *Omd* genotype (Figure 4A and B). More specifically, the increase in cortical thickness could be attributed to augmented periosteal bone accrual as only the outer diameter was significantly larger, while the inner diameter did not change after *Wnt1* induction (Figure 4C). Biomechanically, the thicker cortical compartment translated into improved mechanical stability of the femora from 12-week old female mice after 3 weeks of *Wnt1* induction as assessed in 3-point-bending assays (Figure 4D). Interestingly, after calculation of the flexural strength, it became apparent that the bone matrix material property of $Omd^{+/+}$ mice is not altered by the induction of *Wnt1*. In contrast, the flexural strength calculated for $Omd^{-/-}$ mice was unexpectedly significantly increased after *Wnt1* induction, indicating that OMD may have a direct influence on inherent bone matrix properties or skeletal geometry (Figure 4D).

In order to explore this aspect in more detail, we focused our subsequent investigations on the phenotype of $Omd^{-/-}$ mice independent of WNT1. Setting up matings of *Omd*-heterozygous mice allowed us to compare the phenotype of $Omd^{-/-}$ mice using $Omd^{+/+}$ littermates as controls. Structural histomorphometry of lumbar vertebral spine sections did not indicate significant alterations of the trabecular bone compartment in $Omd^{-/-}$ mice compared with $Omd^{+/+}$ littermates in any of the investigated age/sex groups (Figure 5A and B). Moreover, closer examination of the tibiae revealed comparable results with no significant structural differences in the proximal metaphyseal trabecular compartment (Figure 5C and D).

In line with these observations, *ex vivo* cultured primary bone marrow osteoblasts from $Omd^{+/+}$ and $Omd^{-/-}$ mice showed no difference in mineralized matrix production as determined by alizarin red staining (Figure 6A and B) after 11 and 15 days of osteogenic differentiation. Western blotting and qRT-PCR expression analysis confirmed the absence of OMD in these cells, and we only observed significantly decreased expression of *Runx2* and *Wnt16* in $Omd^{-/-}$ osteoblasts at day 15 of osteogenic differentiation (Figure 6C and D). As WNT16 is a known modulator of cortical bone microarchitecture, we next performed μCT analysis of femora from 12- and 24-week-old female, as well as 12-week-old male $Omd^{-/-}$ and $Omd^{+/+}$ mice in order to assess both trabecular and cortical microarchitecture. Confirming the previous histomorphometry results, we did not observe differences in trabecular bone mass in the femur (Figure 7A and B). Indeed, even a more comprehensive panel of structural parameters did not consistently reveal any relevant differences of the trabecular bone compartment between $Omd^{-/-}$ and $Omd^{+/+}$ mice (Figure S3A). With regard to the cortical compartment of the femora, there was a minor but significant increase in cortical thickness in 12-week-old female $Omd^{-/-}$ mice compared with $Omd^{+/+}$ littermate controls (Figure 7C and D). However, this finding was not reproducible in any of the other analyzed groups. Likewise, there was no difference in cortical porosity, and the overall femoral length was not affected by OMD deficiency (Figure S3A). Likewise, the growth plate thickness and morphology remained unchanged between $Omd^{+/+}$ and $Omd^{-/-}$ mice (Figure S4A and B).

More importantly, we determined a significant decrease of both, inner and outer cortical diameter, in $Omd^{-/-}$ mice compared with their respective $Omd^{+/+}$ controls that was fully consistent throughout all investigated groups (Figure 7C and E). The presence of this slender bone phenotype was further confirmed by similar observations made in tibiae and humeri of $Omd^{-/-}$ mice. While only the tibiae from 12-week-old female mice displayed a significant increase in cortical thickness (Figure 7F and G, Figure S3B), there was consistently a significant decrease of the inner and outer diameter of the cortical shell in the mid-diaphyseal region of both tibia and humerus (Figure 7F and H). On the other hand, results from the μCT-based evaluation of calvarial thickness and porosity showed no significant difference between female $Omd^{-/-}$ and $Omd^{+/+}$ at the age of 12 weeks (Figure S5). These results suggest that the lack of OMD specifically limits transversal but not longitudinal bone growth to cause a slender bone phenotype.

Next, we aimed to investigate if the altered morphology of *Omd*-deficient bones can influence their biomechanical

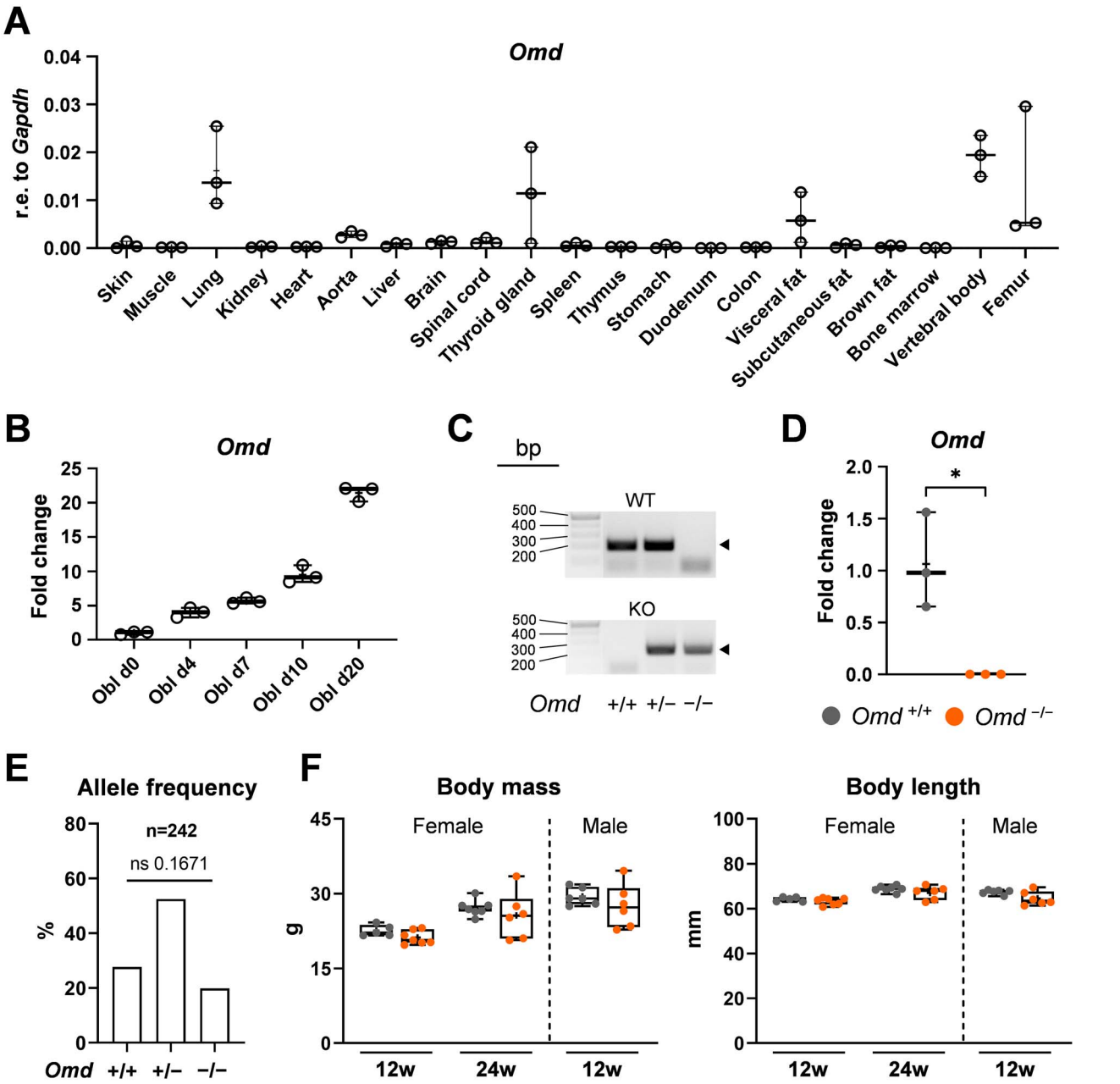

Figure 2. Generation of *Omd*-deficient mice. A) Expression of *Omd* in the indicated tissues from 8-week-old female C57Bl6/J wild-type mice as determined by qRT-PCR. $n = 3$ B) *Omd* expression in murine calvarial osteoblasts throughout osteogenic differentiation. Data are shown relative to day 0 (Obl d0). $n = 3$. C) Representative images of agarose gel electrophoreses (ethidiumbromide stain) with PCR products used for genotyping of the *Omd*-deficiency mouse model. The triangles indicate the position of the expected wildtype (WT) and knockout (KO) PCR products. At the bottom the determined genotypes are indicated. D) Expression of *Omd* in femoral cortex isolated from 7-week-old male and female $Omd^{+/+}$ and $Omd^{-/-}$ mice. $n = 3$. Data are presented as box plots with dots for individual datapoints. Data were analyzed by Student t-test. * $P < .05$, *** $P < .001$. E) Allele frequency chart for 242 offspring mice from heterozygous matings. Data were compared with the expected Mendelian ratio by chi-squared test. F) Body mass and length of 12- and 24-week-old female and 12-week-old male $Omd^{-/-}$ mice compared with their respective $Omd^{+/+}$ littermate controls. Data are presented as box plots with dots for individual datapoints, $n = 5$-7. Data were analyzed by Student t-test.

properties. Therefore, we performed 3-point-bending assays with femora from 12-week-old female mice. Interestingly, despite the reduced transversal dimension of the bones from $Omd^{-/-}$ mice, the bending modulus and maximum resistive force were unaltered (Figure 8A, B, and C). Additionally, the flexural strength was significantly increased in femora of $Omd^{-/-}$ mice (Figure 8C). Based on the geometrical variations between *Omd*-deficient and control mice as reflected by the reduced sections modulus (Figure 8D), these data are in line with a reduced flexural stiffness in $Omd^{-/-}$ mice (Figure 8D). We further applied nanoindentation on tibiae for direct assessment of cortical bone matrix materialproperties in compression. Here we did not observe differences in hardness and elastic modulus (Figure 8E). Taken together, these data indicate unaltered mechanical properties of the bone matrix in $Omd^{-/-}$ mice.

Nonetheless, considering the proposed role of OMD in collagen fibril organization, we subsequently investigated by

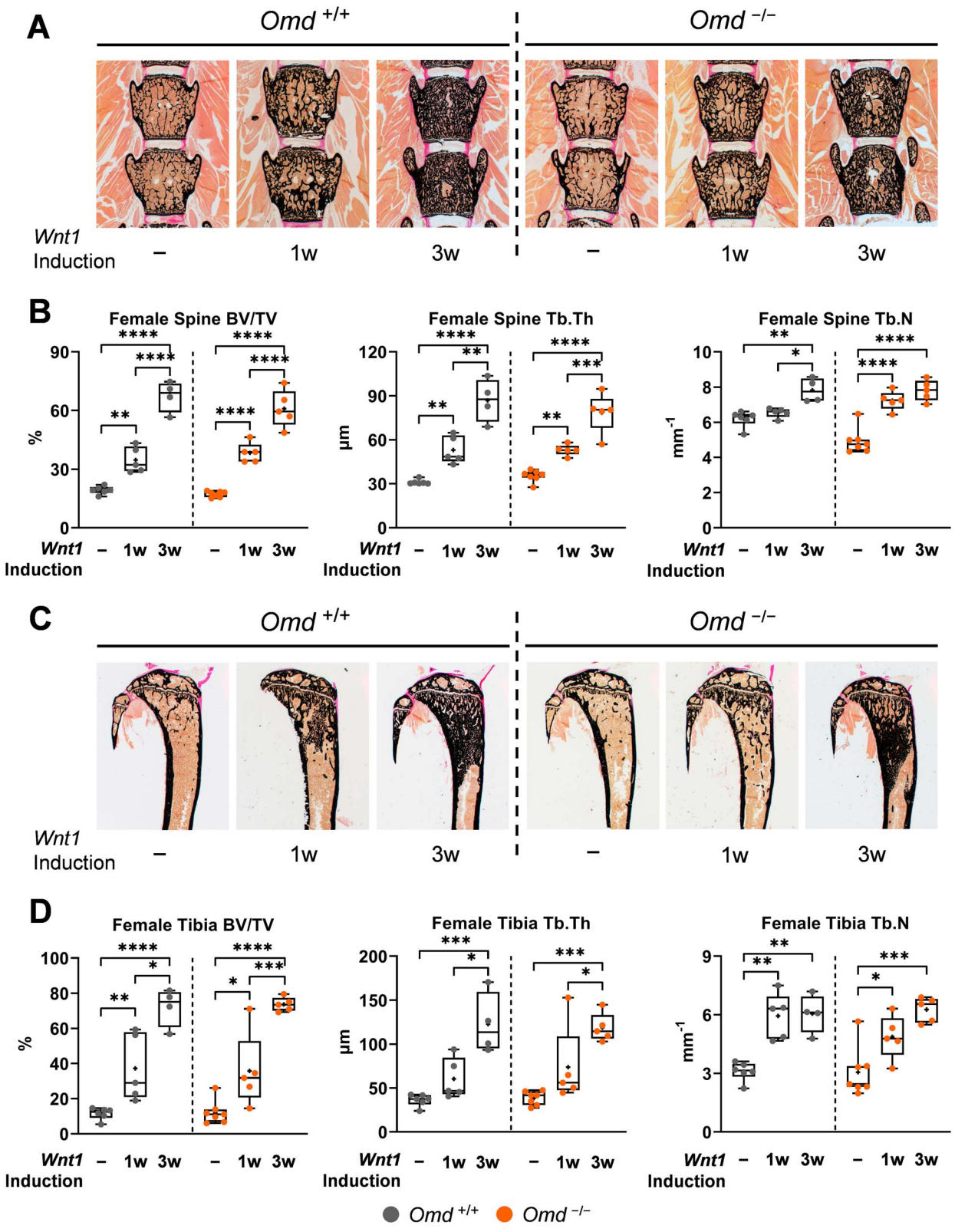

Figure 3. Effect of OMD deficiency on WNT1-induced trabecular bone formation. A) Representative images of the vertebral bodies L3-L4 (van Gieson/von Kossa stain) from 12-week-old, female *Omd*$^{+/+}$ or *Omd*$^{-/-}$ carrying an inducible, osteoblast specific *Wnt1* transgene with no (-), one week (1w), or 3 weeks (3w) of *Wnt1* transgene induction before sacrifice. B) Structural histomorphometric parameters of the vertebral bodies of the indicated animals. C) Representative images of the right tibiae (van Gieson/von Kossa stain) from the same groups of animals as described in subpanel a. D) Structural histomorphometric parameters of the proximal metaphyseal trabecular compartment of the tibiae isolated from the indicated animals. Data are presented as box plots with dots for individual datapoints, $n = 4$-7. Data were analyzed by one-way ANOVA with Tukey's post-hoc test. * $P < .05$, ** $P < .01$, *** $P < .001$, **** $P < .0001$.

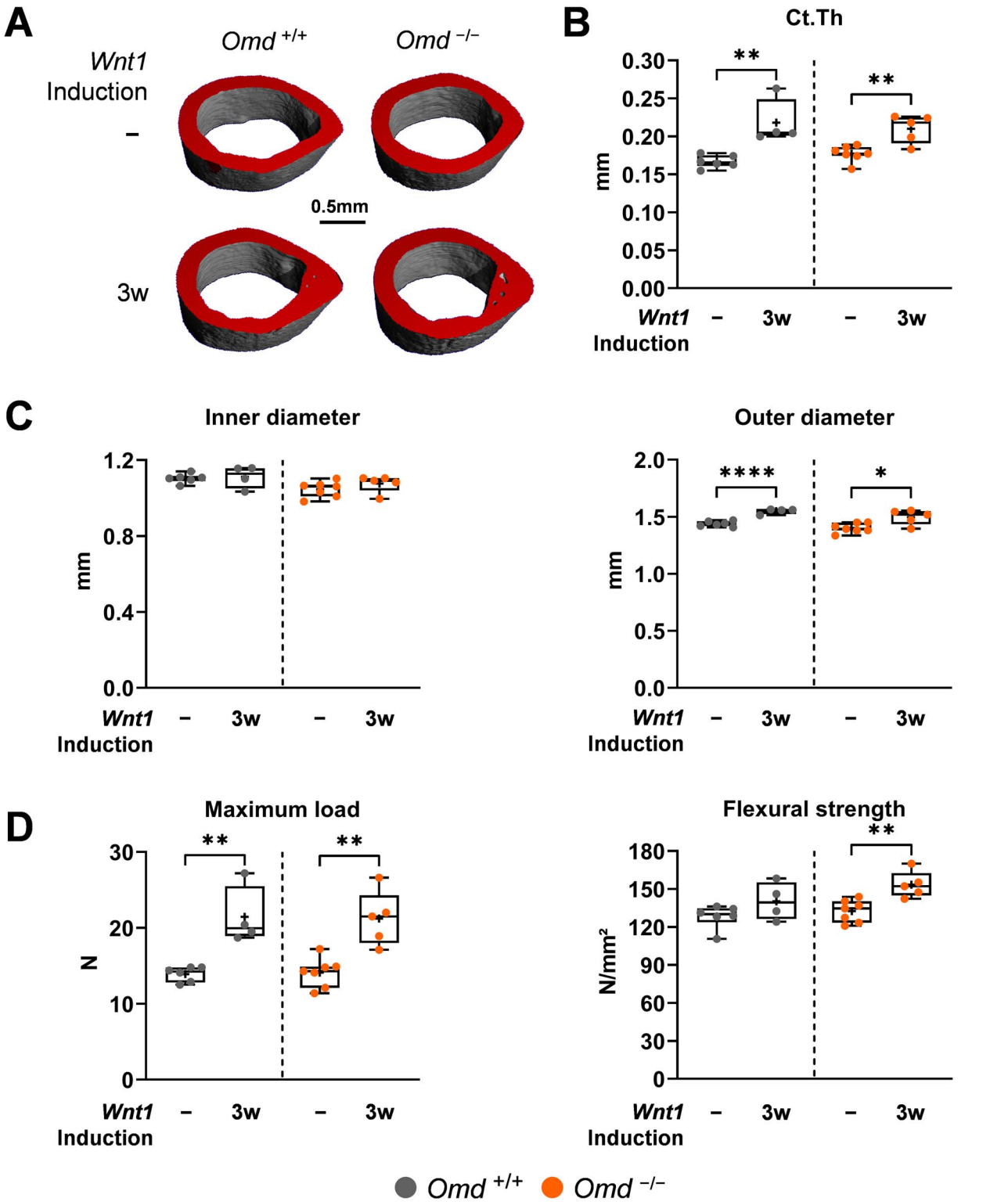

Figure 4. Effect of OMD deficiency on WNT1-induced cortical bone formation and mechanical properties. A) Representative μCT reconstructions of the mid-diaphyseal cortical bone compartment of the right femora from 12-week-old, female *Omd*$^{+/+}$ and *Omd*$^{-/-}$ mice carrying an inducible, osteoblast specific *Wnt1* transgene with no (-) or 3 weeks (3w) induction before sacrifice. Scale bar = 0.5 mm B) μCT-based quantification of the cortical thickness of the mid-diaphyseal cortical compartment of the right femora from 12-week-old female *Omd*$^{+/+}$ or *Omd*$^{-/-}$ mice with (3w) or without (-) 3 weeks induction of the *Wnt1* transgene prior to sacrifice. C) μCT-based quantification of the inner and outer cortical diameter of the mid-diaphyseal cortical compartment of the right femora from 12-week-old female mice with the indicated genotype and *Wnt1*-induction status. D) Maximum force applied and flexural strength of explanted femora from 12-week-old female mice with the indicated *Omd*-genotype and *Wnt1*-induction status as determined during a 3-point-bending test. Data are presented as box plots with dots for individual datapoints, $n = 4$-7. Data were analyzed by Student t-test. * $P < .05$, ** $P < .01$, *** $P < .001$, **** $P < .0001$.

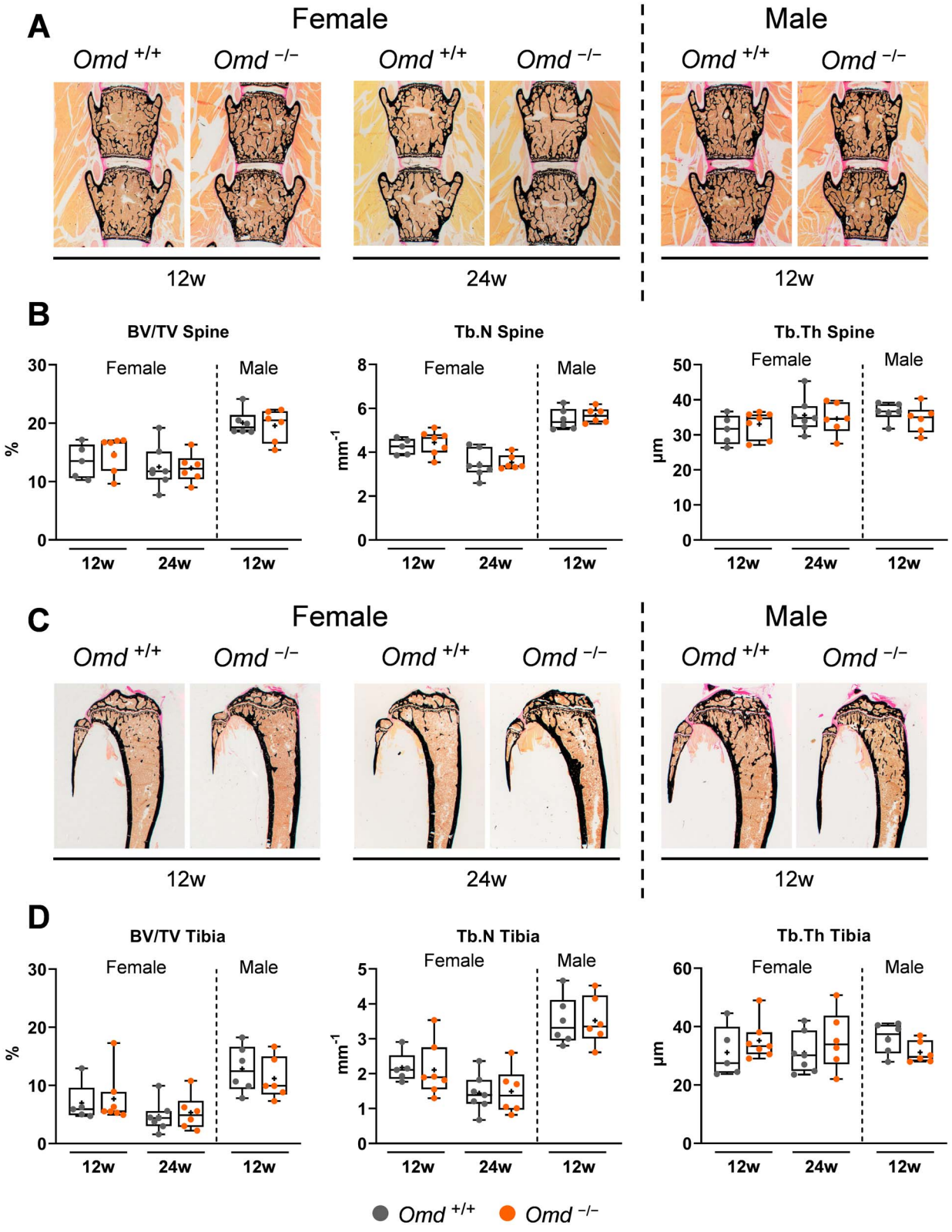

Figure 5. Histomorphometric skeletal phenotype of *Omd*-deficient mice. A) Representative images of the vertebral bodies L3-L4 (van Gieson/von Kossa stain) of mice with the indicated age, gender, and genotype. B) Structural histomorphometric parameters of the vertebral bodies of the indicated animals. C) Representative images of the right tibiae (van Gieson/von Kossa stain) of mice with the indicated age, gender, and genotype. D) Structural histomorphometric parameters of the proximal metaphyseal trabecular compartment from the tibiae of the indicated animals. Data are presented as box plots with dots for individual datapoints, $n = 5$-7. Data were analyzed by Student t-test.

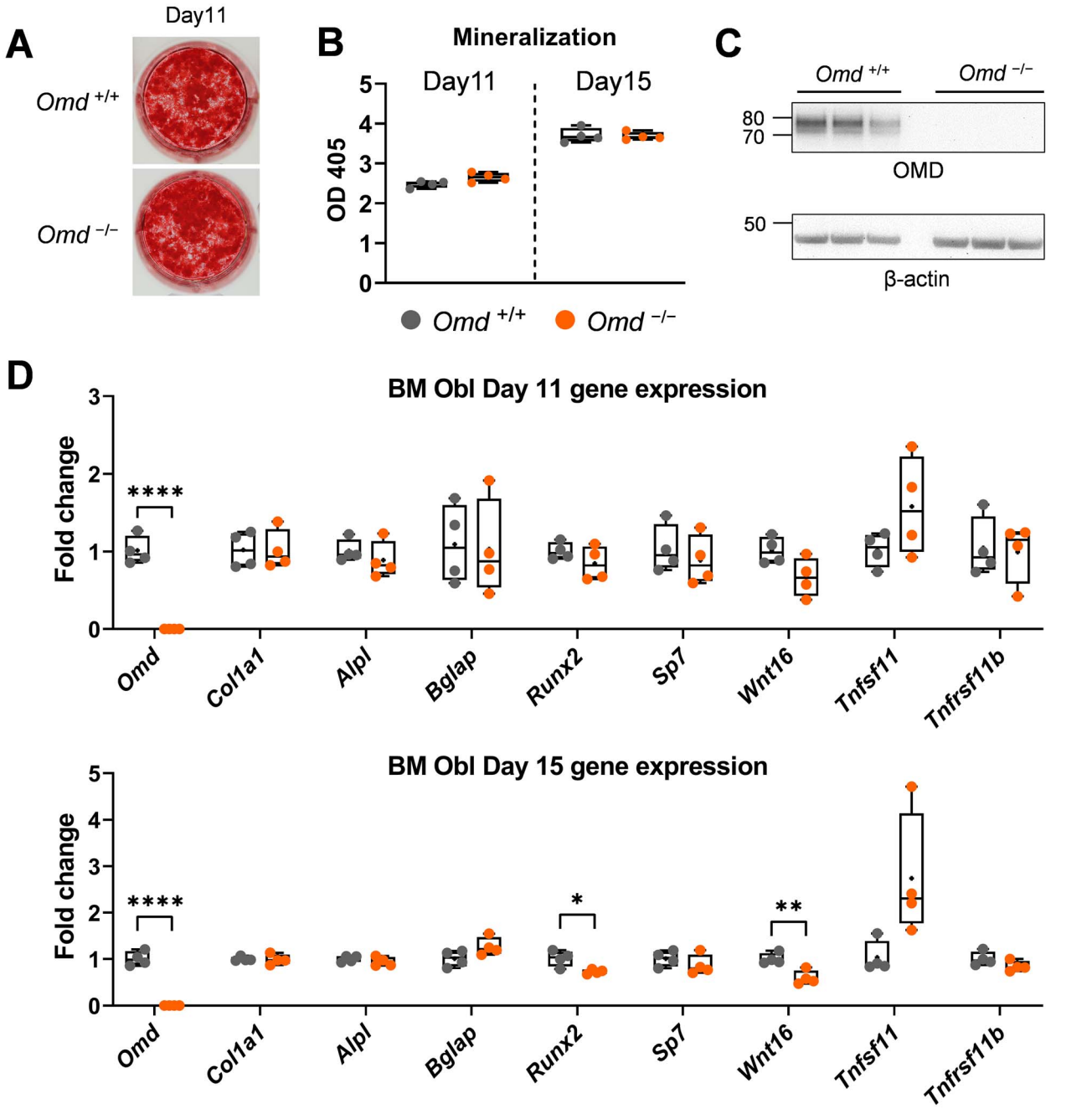

Figure 6. Cell autonomous phenotype of *Omd*-deficient osteoblasts. A) Representative alizarin red stainings of mineralized matrix in bone marrow osteoblast cultures from $Omd^{+/+}$ and $Omd^{-/-}$ mice after 11 days of osteogenic differentiation. B) Quantification of alizarin red stained mineralized matrix in bone marrow osteoblast cultures after 11 and 15 days of osteogenic differentiation. C) Western blot for OMD and β-actin as a loading control in cell lysates of primary bone marrow osteoblast cultures from $Omd^{+/+}$ and $Omd^{-/-}$ mice at day 15 of osteogenic differentiation. D) Gene expression analysis by qRT-PCR of the indicated osteoblast marker genes in primary bone marrow osteoblast cultures from $Omd^{+/+}$ and $Omd^{-/-}$ mice after 11 (upper graph) or 15 (lower graph) days of osteogenic differentiation. Data are presented as box plots with dots for individual datapoints, $n = 4$. Data were analyzed by Student t-test. * $P < .05$, ** $P < .01$, **** $P < .0001$.

polarized light microscopy of the tibial cortical bone if the organization of collagen packets is influenced by the lack of OMD. Here, we observed neither in the lateral nor in the medial cortical region any differences in overall fiber coherency (Figure S6A and B). Similarly, no alteration of the calcium content was detectable by quantitative backscattered electron imaging in the bone matrix of these samples (Figure S6C, D, and E). Therefore, we applied atomic force microscopy to assess nanostructural features of the femoral cortical bone surface. Semiquantitative image classification demonstrated that the bone surface of $Omd^{-/-}$ mice appeared significantly more heterogenous (approx. 15% of images in $Omd^{-/-}$ mice vs. 0% in $Omd^{+/+}$ mice) and less homogenous (approx. 30% of images in $Omd^{-/-}$ mice vs. 60% in $Omd^{+/+}$ mice) than the bone surface of $Omd^{+/+}$ littermate controls (Figure 8F). Indeed, individual collagen fibrils were identifiable in the images, and loosely packed and disorganized fibrils appeared in more than half of the $Omd^{-/-}$ mice, while

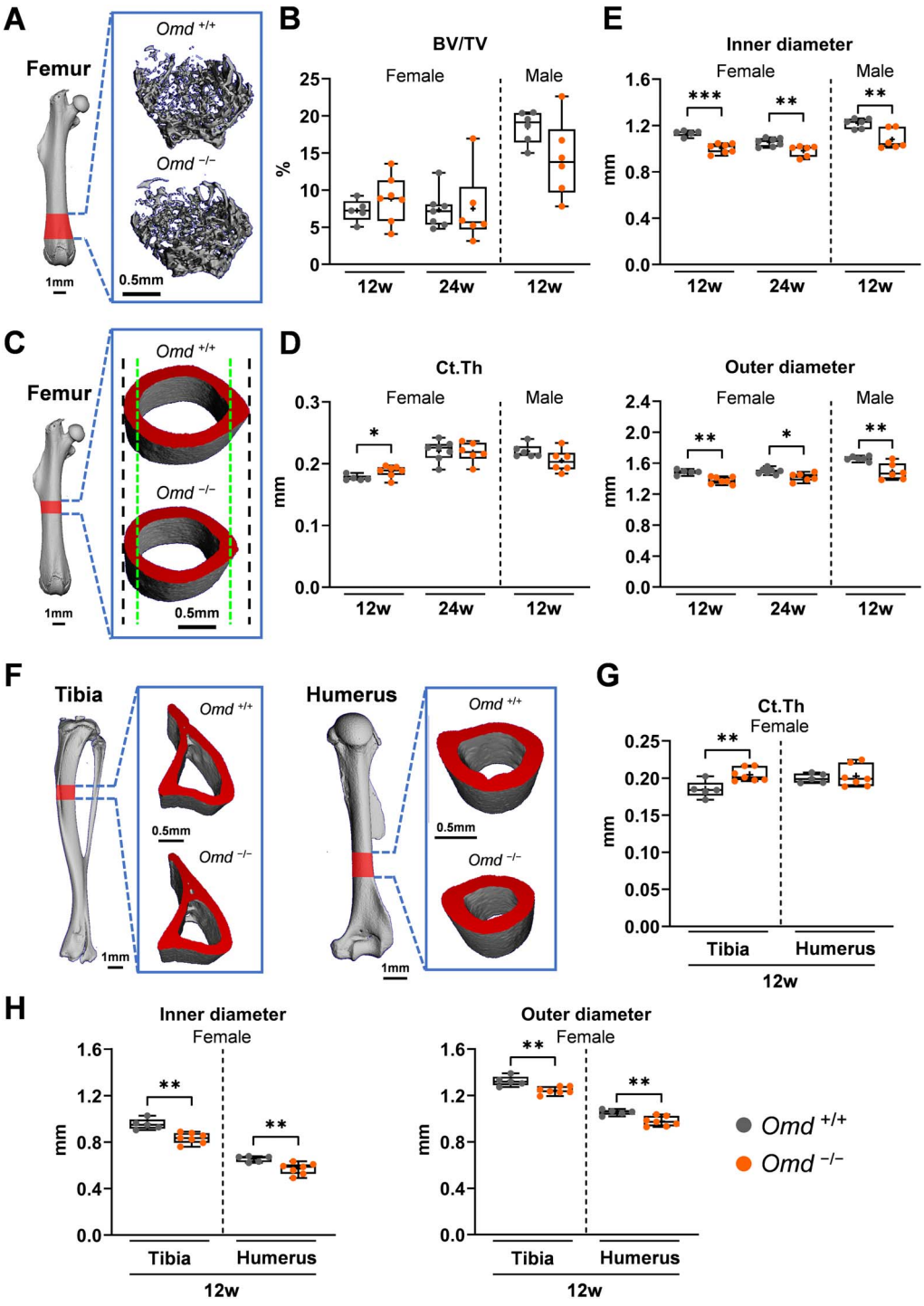

Figure 7. Long bone structural phenotype of *Omd*-deficient mice. A) Representative μCT reconstructions of the distal metaphyseal trabecular bone compartment of the right femora from 12-week-old, female $Omd^{+/+}$ and $Omd^{-/-}$ mice and a full bone representation with the analyzed region of interest indicated in red. Scale bar = 0.5 or 1 mm as indicated. B) μCT-based quantification of the bone volume per tissue volume of the distal metaphyseal trabecular compartment of the right femora from mice with the indicated age, gender, and genotype. C) Representative μCT reconstructions of the mid-diaphyseal cortical bone compartment of the right femora from 12-week-old, female $Omd^{+/+}$ and $Omd^{-/-}$ mice. Black line with long dashes: Outer cortical limit of the $Omd^{+/+}$ sample, green line with short dashes: Inner cortical limit of the $Omd^{+/+}$ sample. Scale bar = 0.5 mm. The red overlay on the full femora depicted on the left indicates the analyzed region of interest. Scale bar = 1 mm. D) μCT-based quantification of the cortical thickness of the mid-diaphyseal cortical compartment of the right femora from mice with the indicated age, gender, and genotype. E) μCT-based quantification of the inner and outer cortical diameter of the mid-diaphyseal cortical compartment of the right femora from mice with the indicated age, gender, and genotype. F) Representative μCT reconstructions of the mid-diaphyseal cortical bone compartment of the left tibiae and humeri from 12-week-old, female $Omd^{+/+}$ and $Omd^{-/-}$ mice, as well as full bone representations with the analyzed regions of interest indicated in red. Scale bar = 0.5 or 1 mm as indicated. G) μCT-based quantification of the cortical thickness of the mid-diaphyseal cortical compartment of the left tibiae and humeri of 12-week-old female $Omd^{+/+}$ and $Omd^{-/-}$ mice. H) μCT-based quantification of the inner and outer cortical diameter of the mid-diaphyseal cortical compartment of the left tibiae and humeri of 12-week-old female $Omd^{+/+}$ and $Omd^{-/-}$ mice. Data are presented as box plots with dots for individual datapoints, $n = 5$-7. Data were analyzed by Student t-test. * $P < .05$, ** $P < .01$, *** $P < .001$.

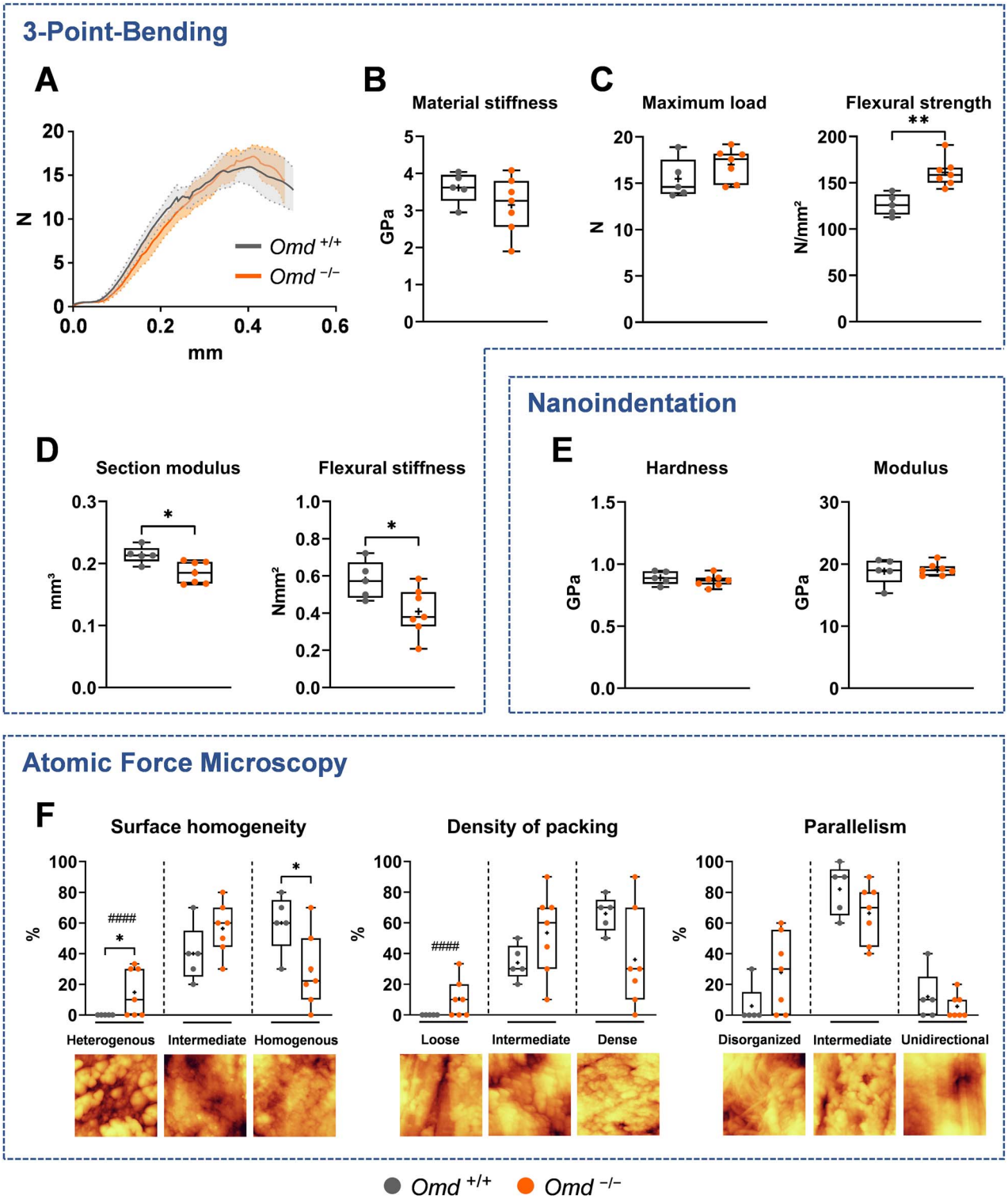

Figure 8. Mechanical and nanostructural properties of *Omd*-deficient bones. A) Load displacement curve of the 3-point-bending assays performed on the explanted femora of 12-week-old female *Omd*$^{+/+}$ and *Omd*$^{-/-}$ mice. The solid lines represent the mean value; the shaded areas denote the standard deviation. $n = 5$ (*Omd*$^{+/+}$), 7 (*Omd*$^{-/-}$). B) Material stiffness, C) maximum force applied, flexural strength, D) section modulus (derived from μCT data), and flexural stiffness as determined by the 3-point-bending test in combination with μCT evaluation for geometric parameters. E) Evaluation of bone matrix material hardness and modulus by nanoindentation. Testing was performed on the cortical compartment of tibiae from 12-week-old female *Omd*$^{+/+}$ and *Omd*$^{-/-}$ mice. F) Nanostructural assessment of femoral surface by atomic force microscopy. Semi-quantitative evaluation of surface homogeneity, fibril density, and parallelism in samples from 12-week-old female *Omd*$^{+/+}$ and *Omd*$^{-/-}$ mice. Data are given as percentage of images per animal with the indicated feature classification (10 images per animal). Representative images (2x2 μm) for the different nanostructural features are shown underneath the graphs. Data are presented as box plots with dots for individual datapoints, $n = 5$-7 animals per group. * $P < .05$, ** $P < .01$. Data were analyzed by Student t-test or Welch t-test if there was a significant difference in variance (F-test, $P < .05$ indicated by ####).

these features were basically absent in $Omd^{+/+}$ mice with the exception of a single animal, where some disorganized fibrils could be identified (Figure 8F). However, although the variance of loosely packed fibrils was significantly higher in $Omd^{-/-}$ samples than in $Omd^{+/+}$ samples, the difference between means did not reach statistical significance and no differences with regard to fibril parallelism were detectable. Nonetheless, these data indicate the presence of overall altered collagen nanostructural organization in $Omd^{-/-}$ mice.

In summary, while OMD is not a major contributor to the osteoanabolic effect of WNT1, our data show that it influences cortical bone geometry in the transversal dimension as well as collagen fibril organization.

Discussion

Osteomodulin is a proteoglycan that is produced by osteoblasts and has been identified as a component of the bone matrix.[15] In vitro studies suggested that it modulates the thickness and branching of type I Collagen fibrils. However, the physiological role of OMD remains elusive, and only very limited in vivo data are currently available. As we observed a strong induction of *Omd* expression in osteoblastic cells in response to the bone anabolic ligand WNT1,[12] we set out to explore the potential influence of OMD on bone physiology in general and more specifically its potential role as a WNT1 downstream mediator. To achieve this goal, we obtained an *Omd*-deficient mouse line and first crossed it with a mouse line harboring an osteoblast specific, inducible *Wnt1* transgene.[6] Subsequent skeletal phenotyping revealed that loss of OMD did not influence the osteoanabolic capacity of WNT1. However, we noted that OMD deficiency appeared to change the mechanical properties of the bone matrix after *Wnt1* induction. To explore this aspect and to generally expand the available knowledge on the physiological function of OMD, we performed extended skeletal phenotyping of *Omd*-deficient mice. We observed that *Omd*-deficient mice displayed a slender bone phenotype with significantly smaller long bones in the transversal dimension, while the longitudinal bone growth remained unaffected. This effect was attributable to decreased inner and outer cortical diameters, whereas cortical thickness remained unaffected in most of the analyzed groups. In contrast, trabecular bone density was not affected by OMD deficiency.

Analysis of the bone surface by atomic force microscopy indicated moderate nanostructural differences in bones from *Omd*-deficient mice compared with wild-type littermate controls. More specifically, loosely packed and disorganized fibrils as well as a heterogenous bone surface appearance were detectable in most *Omd*-deficient samples, while such features were virtually absent in wild-type controls. This suggests a diminished control of collagen apposition, reflected by the significantly higher variance observed in $Omd^{-/-}$ mice that in turn was likely the reason for the lack of statistically significant differences between the mean values. Surprisingly, despite these observed morphological changes on the macroscopic and nanostructural level, the mechanical strength of femora from *Omd*-deficient mice as well as their inherent bone material properties remained unaltered. The nanostructural phenotype is likely too mild to significantly alter the material properties of the bone matrix. Thus, the smaller diameter and negligible differences in cortical thickness of the long bones actually led to improved flexural strength as expected from a purely mechanical consideration of the geometric properties, as is apparent.

Interestingly, despite its abundance in the bone matrix and similar distribution to bone sialoprotein,[38] research efforts to elucidate the physiological role of OMD have been limited. Indeed, only in a very recent study the potential in vivo functions of OMD were described for the first time.[22] More specifically, the authors compared the effects of *Omd* deficiency and overexpression in mice with a specific focus on cartilage, where they found indications that OMD may have a protective effect against the development of osteoarthritis.[22] Moreover, evaluation of tibial metaphysis revealed a decrease in trabecular bone density specifically in *Omd*-overexpressing mice at 8 months of age, while OMD deficiency had no appreciable effect. These results are in line with our own observations, where we did not detect an effect of OMD deficiency on trabecular bone parameters of vertebral bodies, tibiae and femora. Similarly, the authors described an increased cortical thickness in *Omd*-deficient mice that we observed likewise, although only in 12-week-old female animals. Based on additional zebrafish and in vitro studies, the authors proposed that the positive effect of OMD on bone mass is mediated via direct binding and sequestering of Rankl, a highly relevant factor inducing the differentiation of osteoclasts. Indeed, another study showed that osteoblastic expression of *Omd* is dependent on the presence of osteoclasts, as M-CSF-deficient mice had diminished OMD levels that were recovered by M-CSF treatment.[39] While these studies suggest a role of OMD in osteoclast–osteoblast crosstalk, other in vitro studies have shown a positive regulation of osteoblast activity by OMD. Here, a beneficial influence of OMD on in vitro differentiation and mineralization was described in MC3T3-E1 cells.[18] This effect might be partially attributable to OMD-mediated regulation of apoptosis and growth.[19] Furthermore, BMP2 has been shown to induce *Omd* expression,[19,40] and *vice versa* OMD has been described to potentiate the effect of BMP2 by direct molecular interaction.[21] Therefore, although the cellular and molecular functions of OMD still remain to be fully characterized, most experimental evidence obtained so far indicates an effect of OMD on osteoblast activity. Considering the specific effect of OMD deficiency on cortical geometry that we observed persistently in all age groups, we are inclined to consider osteoblastic activity as the most likely underlying cellular mechanism. Therefore, this phenotype may also be the consequence of altered bone development, similar to the cortical phenotype of Plastin3-deficient mice that we have described previously.[41] Indeed, while bone marrow-derived primary osteoblasts did not have a cell-autonomous mineralization phenotype in our investigation, we did observe a decreased expression of *Wnt16*, encoding a ligand that specifically supports cortical bone accrual,[42] suggesting a potential molecular link between OMD deficiency and cortical bone geometry.

On a molecular level, there is convincing in vitro evidence that a major function of OMD is the regulation of collagen fibril diameter and branching. Interaction studies of recombinant OMD with purified type I collagen have shown that OMD reduces the diameter and smoothens the shape of self-assembling collagen fibrils.[16] Indeed, it was shown that repeated binding of OMD to type I collagen essentially slows the fibril formation process, allowing for the assembly of more uniform fibrils with less branching and kinking.[17]

This mechanism is in agreement with our *ex vivo* evaluation of bone surface fibrils by atomic force microscopy. While our data have to be considered with the caveat that we did not assess pure collagen but rather mineralized bone matrix, we did observe tendencies toward less densely and more chaotically packed fibrils and a generally more heterogenous cortical bone surface in *Omd*-deficient mice, supported by the significantly higher variance of these parameters compared with the littermate controls. Thus, our findings confirm the hypothesis that lack of OMD results in decreased regulation and control of collagen fibril arrangement.

There are some limitations to this study. While we were able to discover new aspects of the physiological influence of OMD on the skeleton, our elucidation of the underlying mechanisms remains mostly speculative and based on circumstantial evidence. Therefore, future studies may focus on younger animals, in order to substantiate the hypothesis that the cortical phenotype manifests during development. Although we have tested the hardness of the bone matrix of *Omd*-deficient mice by nanoindentation, this parameter is predominantly influenced by the mineral phase and a potential influence of *Omd*-deficiency on tensile strength cannot be fully excluded. Moreover, there are some additional, partially extra-skeletal, physiological aspects related to OMD activity that we did not investigate as they were beyond the scope of this study. For example, potential functions of OMD have been suggested for dental development and homeostasis, specifically in odontoblasts in dental pulp.[20,43-47] Likewise, there are some recent studies that indicate a function of OMD in the context of cardiovascular disorders. More specifically, there is evidence that OMD is a protective factor during plaque calcification, as it attenuates the osteogenic transition of smooth muscle cells.[48-50] Finally, although *Omd*-deficiency did not impair the osteoanabolic function of WNT1 in vivo, our findings in mesenchymal ST2 cells raise the relevant question that remains to be addressed in future studies: which cell types are responding to WNT1 after inducible expression in osteoblasts?

In conclusion, our data clearly demonstrate that OMD is dispensable for the osteoanabolic effect of WNT1. Additionally, they provide direct in vivo insights into the physiological role of OMD by skeletal phenotyping of *Omd*-deficient mice. In fact, lack of OMD causes altered cortical geometry, specifically a slender bone phenotype with smaller transversal diameters of long bones, while trabecular bone remained unaffected. Furthermore, we observed moderate cortical nanostructural changes in line with altered collagen fibril organization. Therefore, this study provides the first in vivo evidence to support the hypothesis that OMD regulates the shape of type I collagen fibrils.

Acknowledgments

We thank the UKE research animal facility for their excellent services. Moreover, we would like to express our gratitude to Olga Winter, Mona Neven, Lana Rosenthal, Andrea Thieke, and Annette Jung for their technical assistance.

Author contributions

Thorsten Schinke, Timur A. Yorgan (Conceptualization), Wenbo Zhao, Simon von Kroge, Petar Milovanovic, Praveer Sihota, Julia Luther, Laura Brylka, Felix N. von Brackel, Ernesto Bockamp, Björn Busse, Michael Amling, Thorsten Schinke, Timur A. Yorgan (Methodology), Wenbo Zhao, Thorsten Schinke, Timur A. Yorgan (Validation), Wenbo Zhao, Petar Milovanovic, Felix N. von Brackel, Timur A. Yorgan (Formal analysis), Wenbo Zhao, Simon von Kroge, Jelena Jadzic, Petar Milovanovic, Praveer Sihota, Julia Luther, Laura Brylka, Timur A. Yorgan (Investigation), Petar Milovanovic, Ernesto Bockamp, Björn Busse, Michael Amling, Thorsten Schinke, Timur A. Yorgan (Resources), Wenbo Zhao, Timur A. Yorgan (Data Curation), Thorsten Schinke, Timur A. Yorgan (Writing—original draft), all authors (Writing—review & editing), Wenbo Zhao, Thorsten Schinke, Timur A. Yorgan (Visualization), Thorsten Schinke, Timur A. Yorgan (Supervision), Timur A. Yorgan (Project administration), and Thorsten Schinke, Timur A. Yorgan (Funding acquisition)

Supplementary material

Supplementary material is available at *Journal of Bone and Mineral Research* online.

Funding

The work was supported by grants from the Deutsche Forschungsgemeinschaft (SCHI 504/15-1 and YO 299/2-1). W.Z. received funding through the China Scholarship Council. P.M. and J.J. acknowledge support from the Ministry of Science of Republic of Serbia and the Science Fund of Republic of Serbia (BoFraM). P.M. and B.B. acknowledge support from the Alexander von Humboldt Foundation.

Conflicts of interest

All authors state that they have no conflict of interest.

Data availability

All relevant data are present in the manuscript; raw data are available upon request from the corresponding authors; microarray data are available in the GEO repository.

References

1. Katsimbri P. The biology of normal bone remodelling. *Eur J Cancer Care (Engl)*. 2017;26(6):1–5. https://doi.org/10.1111/ecc.12740
2. Capulli M, Paone R, Rucci N. Osteoblast and osteocyte: games without frontiers. *Arch Biochem Biophys*. 2014;561:3–12. https://doi.org/10.1016/j.abb.2014.05.003
3. Teitelbaum SL. Bone resorption by osteoclasts. *Science*. 2000;289(5484):1504–1508. https://doi.org/10.1126/science.289.5484.1504
4. Compston JE, McClung MR, Leslie WD. Osteoporosis. *Lancet*. 2019;393(10169):364–376. https://doi.org/10.1016/S0140-6736(18)32112-3
5. Langdahl BL. Overview of treatment approaches to osteoporosis. *Br J Pharmacol*. 2021;178(9):1891–1906. https://doi.org/10.1111/bph.15024
6. Luther J, Yorgan TA, Rolvien T, et al. Wnt1 is an Lrp5-independent bone-anabolic Wnt ligand. *Sci Transl Med*. 2018;10(466):1–12. https://doi.org/10.1126/scitranslmed.aau7137
7. Keupp K, Beleggia F, Kayserili H, et al. Mutations in WNT1 cause different forms of bone fragility. *Am J Hum Genet*. 2013;92(4):565–574. https://doi.org/10.1016/j.ajhg.2013.02.010
8. Laine CM, Joeng KS, Campeau PM, et al. WNT1 mutations in early-onset osteoporosis and osteogenesis imperfecta. *N Engl J Med*. 2013;368(19):1809–1816. https://doi.org/10.1056/NEJMoa1215458
9. Pyott SM, Tran TT, Leistritz DF, et al. WNT1 mutations in families affected by moderately severe and progressive recessive osteogenesis imperfecta. *Am J Hum Genet*. 2013;92(4):590–597. https://doi.org/10.1016/j.ajhg.2013.02.009

10. Fahiminiya S, Majewski J, Mort J, Moffatt P, Glorieux FH, Rauch F. Mutations in WNT1 are a cause of osteogenesis imperfecta. *J Med Genet*. 2013;50(5):345–348. https://doi.org/10.1136/jmedgenet-2013-101567
11. Yorgan TA, Rolvien T, Sturznickel J, et al. Mice carrying a ubiquitous R235W mutation of Wnt1 display a bone-specific phenotype. *J Bone Miner Res*. 2020;35(9):1726–1737. https://doi.org/10.1002/jbmr.4043
12. Vollersen N, Zhao W, Rolvien T, et al. The WNT1(G177C) mutation specifically affects skeletal integrity in a mouse model of osteogenesis imperfecta type XV. *Bone Res*. 2021;9(1):48. https://doi.org/10.1038/s41413-021-00170-0
13. Joeng KS, Lee YC, Lim J, et al. Osteocyte-specific WNT1 regulates osteoblast function during bone homeostasis. *J Clin Invest*. 2017;127(7):2678–2688. https://doi.org/10.1172/JCI92617
14. Wang F, Tarkkonen K, Nieminen-Pihala V, et al. Mesenchymal cell-derived Juxtacrine Wnt1 Signaling regulates osteoblast activity and osteoclast differentiation. *J Bone Miner Res*. 2019;34(6):1129–1142. https://doi.org/10.1002/jbmr.3680
15. Wendel M, Sommarin Y, Heinegard D. Bone matrix proteins: isolation and characterization of a novel cell-binding keratan sulfate proteoglycan (osteoadherin) from bovine bone. *J Cell Biol*. 1998;141(3):839–847. https://doi.org/10.1083/jcb.141.3.839
16. Tashima T, Nagatoishi S, Sagara H, Ohnuma S, Tsumoto K. Osteomodulin regulates diameter and alters shape of collagen fibrils. *Biochem Biophys Res Commun*. 2015;463(3):292–296. https://doi.org/10.1016/j.bbrc.2015.05.053
17. Tashima T, Nagatoishi S, Caaveiro JMM, et al. Molecular basis for governing the morphology of type-I collagen fibrils by Osteomodulin. *Commun Biol*. 2018;1(1):33. https://doi.org/10.1038/s42003-018-0038-2
18. Rehn AP, Cerny R, Sugars RV, Kaukua N, Wendel M. Osteoadherin is upregulated by mature osteoblasts and enhances their in vitro differentiation and mineralization. *Calcif Tissue Int*. 2008;82(6):454–464. https://doi.org/10.1007/s00223-008-9138-1
19. Hamaya E, Fujisawa T, Tamura M. Osteoadherin serves roles in the regulation of apoptosis and growth in MC3T3-E1 osteoblast cells. *Int J Mol Med*. 2019;44(6):2336–2344. https://doi.org/10.3892/ijmm.2019.4376
20. Lin W, Gao L, Jiang W, et al. The role of osteomodulin on osteo/odontogenic differentiation in human dental pulp stem cells. *BMC Oral Health*. 2019;19(1):22. https://doi.org/10.1186/s12903-018-0680-6
21. Lin W, Zhu X, Gao L, Mao M, Gao D, Huang Z. Osteomodulin positively regulates osteogenesis through interaction with BMP2. *Cell Death Dis*. 2021;12(2):147. https://doi.org/10.1038/s41419-021-03404-5
22. Zappia J, Tong Q, Van der Cruyssen R, et al. Osteomodulin down-regulation is associated with osteoarthritis development. *Bone Res*. 2023;11(1):49. https://doi.org/10.1038/s41413-023-00286-5
23. Peng J, Bencsik M, Louie A, et al. Conditional expression of a Gi-coupled receptor in osteoblasts results in trabecular osteopenia. *Endocrinology*. 2008;149(3):1329–1337. https://doi.org/10.1210/en.2007-0235
24. Gunther EJ, Moody SE, Belka GK, et al. Impact of p53 loss on reversal and recurrence of conditional Wnt-induced tumorigenesis. *Genes Dev*. 2003;17(4):488–501. https://doi.org/10.1101/gad.1051603
25. Zhao W, Wiedemann P, Wolfel EM, et al. Decreased trabecular bone mass in Col22a1-deficient mice. *Cells*. 2021;10(11):1–15. https://doi.org/10.3390/cells10113020
26. Albers J, Schulze J, Beil FT, et al. Control of bone formation by the serpentine receptor Frizzled-9. *J Cell Biol*. 2011;192(6):1057–1072. https://doi.org/10.1083/jcb.201008012
27. Edgar R, Domrachev M, Lash AE. Gene expression omnibus: NCBI gene expression and hybridization array data repository. *Nucleic Acids Res*. 2002;30(1):207–210. https://doi.org/10.1093/nar/30.1.207
28. Albers J, Keller J, Baranowsky A, et al. Canonical Wnt signaling inhibits osteoclastogenesis independent of osteoprotegerin. *J Cell Biol*. 2013;200(4):537–549. https://doi.org/10.1083/jcb.201207142
29. Dempster DW, Compston JE, Drezner MK, et al. Standardized nomenclature, symbols, and units for bone histomorphometry: a 2012 update of the report of the ASBMR Histomorphometry nomenclature committee. *J Bone Miner Res*. 2013;28(1):2–17. https://doi.org/10.1002/jbmr.1805
30. Schneider CA, Rasband WS, Eliceiri KW. NIH image to ImageJ: 25 years of image analysis. *Nat Methods*. 2012;9(7):671–675. https://doi.org/10.1038/nmeth.2089
31. Rezakhaniha R, Agianniotis A, Schrauwen JT, et al. Experimental investigation of collagen waviness and orientation in the arterial adventitia using confocal laser scanning microscopy. *Biomech Model Mechanobiol*. 2012;11(3-4):461–473. https://doi.org/10.1007/s10237-011-0325-z
32. Oheim R, Zimmerman K, Maulding ND, et al. Human heterozygous ENPP1 deficiency is associated with early onset osteoporosis, a phenotype recapitulated in a mouse model of Enpp1 deficiency. *J Bone Miner Res*. 2020;35(3):528–539. https://doi.org/10.1002/jbmr.3911
33. Yorgan TA, Peters S, Jeschke A, et al. The anti-Osteoanabolic function of Sclerostin is blunted in mice carrying a high bone mass mutation of Lrp5. *J Bone Miner Res*. 2015;30(7):1175–1183. https://doi.org/10.1002/jbmr.2461
34. Bouxsein ML, Boyd SK, Christiansen BA, Guldberg RE, Jepsen KJ, Muller R. Guidelines for assessment of bone microstructure in rodents using micro-computed tomography. *J Bone Miner Res*. 2010;25(7):1468–1486. https://doi.org/10.1002/jbmr.141
35. Oliver WC, Pharr GM. An improved technique for determining hardness and elastic-modulus using load and displacement sensing indentation experiments. *J Mater Res*. 1992;7(6):1564–1583. https://doi.org/10.1557/JMR.1992.1564
36. Faul F, Erdfelder E, Buchner A, Lang AG. Statistical power analyses using G*power 3.1: tests for correlation and regression analyses. *Behav Res Methods*. 2009;41(4):1149–1160. https://doi.org/10.3758/BRM.41.4.1149
37. Kreft L, Soete A, Hulpiau P, Botzki A, Saeys Y, De Bleser P. ConTra v3: a tool to identify transcription factor binding sites across species, update 2017. *Nucleic Acids Res*. 2017;45(W1):W490–W494. https://doi.org/10.1093/nar/gkx376
38. Ramstad VE, Franzen A, Heinegard D, Wendel M, Reinholt FP. Ultrastructural distribution of osteoadherin in rat bone shows a pattern similar to that of bone sialoprotein. *Calcif Tissue Int*. 2003;72(1):57–64. https://doi.org/10.1007/s00223-002-2047-9
39. Ninomiya K, Miyamoto T, Imai J, et al. Osteoclastic activity induces osteomodulin expression in osteoblasts. *Biochem Biophys Res Commun*. 2007;362(2):460–466. https://doi.org/10.1016/j.bbrc.2007.07.193
40. Rehn AP, Chalk AM, Wendel M. Differential regulation of osteoadherin (OSAD) by TGF-beta1 and BMP-2. *Biochem Biophys Res Commun*. 2006;349(3):1057–1064. https://doi.org/10.1016/j.bbrc.2006.08.133
41. Yorgan TA, Sari H, Rolvien T, Windhorst S, Failla AV, Kornak U, Oheim R, Amling M, Schinke T Mice lacking plastin-3 display a specific defect of cortical bone acquisition. *Bone* Jan 2020;130(1):115062, https://doi.org/10.1016/j.bone.2019.115062.
42. Moverare-Skrtic S, Henning P, Liu X, et al. Osteoblast-derived WNT16 represses osteoclastogenesis and prevents cortical bone fragility fractures. *Nat Med*. 2014;20(11):1279–1288. https://doi.org/10.1038/nm.3654
43. Buchaille R, Couble ML, Magloire H, Bleicher F. Expression of the small leucine-rich proteoglycan osteoadherin/osteomodulin in human dental pulp and developing rat teeth. *Bone*. 2000;27(2):265–270. https://doi.org/10.1016/S8756-3282(00)00310-0

44. Nikdin H, Olsson ML, Hultenby K, Sugars RV. Osteoadherin accumulates in the predentin towards the mineralization front in the developing tooth. *PLoS One*. 2012;7(2):e31525. https://doi.org/10.1371/journal.pone.0031525
45. Petersson U, Hultenby K, Wendel M. Identification, distribution and expression of osteoadherin during tooth formation. *Eur J Oral Sci*. 2003;111(2):128–136. https://doi.org/10.1034/j.1600-0722.2003.00027.x
46. Couble ML, Bleicher F, Farges JC, et al. Immunodetection of osteoadherin in murine tooth extracellular matrices. *Histochem Cell Biol*. 2004;121(1):47–53. https://doi.org/10.1007/s00418-003-0608-2
47. Lucchini M, Romeas A, Couble ML, Bleicher F, Magloire H, Farges JC. TGF beta 1 signaling and stimulation of osteoadherin in human odontoblasts in vitro. *Connect Tissue Res*. 2002;43(2-3):345–353. https://doi.org/10.1080/03008200290000790
48. Nashel DJ. Is atherosclerosis a complication of long-term corticosteroid treatment? *Am J Med*. 1986;80(5):925–929. https://doi.org/10.1016/0002-9343(86)90639-X
49. Guo W, Feng W, Fan X, Huang J, Ou C, Chen M. Osteomodulin is a potential genetic target for hypertrophic cardiomyopathy. *Biochem Genet*. 2021;59(5):1185–1202. https://doi.org/10.1007/s10528-021-10050-1
50. Goncalves I, Oduor L, Matthes F, et al. Osteomodulin gene expression is associated with plaque calcification, stability, and fewer cardiovascular events in the CPIP cohort. *Stroke*. 2022;53(3):e79–e84. https://doi.org/10.1161/STROKEAHA.121.037223